



Microstructure and electrical characterizations of yttrium oxide and yttrium silicate thin films deposited by pulsed liquid-injection plasma-enhanced metal-organic chemical vapor deposition

C. Durand, C. Dubourdieu, Christophe Vallée, V. Loup, M. Bonvalot, O. R. Joubert, Hervé Roussel, O. Renault

► To cite this version:

C. Durand, C. Dubourdieu, Christophe Vallée, V. Loup, M. Bonvalot, et al.. Microstructure and electrical characterizations of yttrium oxide and yttrium silicate thin films deposited by pulsed liquid-injection plasma-enhanced metal-organic chemical vapor deposition. *Journal of Applied Physics*, 2004, 96 (3), pp.1719-1729. <10.1063/1.1766412>. <hal-00390405>

HAL Id: hal-00390405

<https://hal.science/hal-00390405v1>

Submitted on 17 Mar 2023

HAL is a multi-disciplinary open access archive for the deposit and dissemination of scientific research documents, whether they are published or not. The documents may come from teaching and research institutions in France or abroad, or from public or private research centers.

L'archive ouverte pluridisciplinaire **HAL**, est destinée au dépôt et à la diffusion de documents scientifiques de niveau recherche, publiés ou non, émanant des établissements d'enseignement et de recherche français ou étrangers, des laboratoires publics ou privés.



Distributed under a Creative Commons CC BY 4.0 - Attribution - International License

Microstructure and electrical characterizations of yttrium oxide and yttrium silicate thin films deposited by pulsed liquid-injection plasma-enhanced metal-organic chemical vapor deposition

C. Durand^{a)}

Laboratoire des Technologies de la Microélectronique (LTM/CNRS), 17 Avenue des Martyrs (CEA-LETI), 38054 Grenoble Cedex 9, France

C. Dubourdieu

Laboratoire des Matériaux et du Génie Physique, UMR-CNRS 5628, ENSPG, Boîte Postale 46, 38402 Saint Martin d'Hères Cedex, France

C. Vallée, V. Loup, M. Bonvalot, and O. Joubert

Laboratoire des Technologies de la Microélectronique (LTM/CNRS), 17 Avenue de Martyrs (CEA-LETI), 38054 Grenoble Cedex 9, France

H. Roussel

Laboratoire des Matériaux et du Génie Physique, UMR-CNRS 5628, ENSPG, Boîte Postale 46, 38402 Saint Martin d'Hères Cedex, France

O. Renault

CEA-DRT-LETI/DPTS, CEA-Grenoble, 17 Avenue Des Martyrs, 38054 Grenoble Cedex 9, France

Results on yttrium oxide and yttrium silicate films elaborated by an innovative metal-organic chemical vapor deposition process combining plasma assistance and a liquid precursor supply setup are presented. Plasma assistance enables deposition at a much lower substrate temperature and the pulsed-liquid precursor source allows an accurate control of the injected reactive species. According to x-ray photoelectron spectroscopy (XPS) analyses, we show that ultrathin yttrium oxide deposition can be performed at temperature less than 380 °C. Yttrium oxide films contain carbon contamination that can be reduced by increasing the deposition temperature. The plasma plays a key role in the deposition mechanisms and thus in the chemical structure of the films and of the interface. It is shown that the injection frequency, i.e., the reactive species incoming frequency, plays a significant role in the silicate and interface formation. A detailed study is presented using angle-resolved XPS. A high injection frequency limits the formation of SiO₂ interfacial layer and also of the silicate and favors the growth of yttrium oxide. In addition, silicate formation also depends on the deposition temperature. Electrical results show that as-deposited film at 350 °C has a low leakage current ($J < 10^{-7}$ A/cm²) and a high breakdown field (~ 8 M V / c m).

I. INTRODUCTION

Materials with high dielectric constant have been introduced in integrated circuits as stated in the International Technology Roadmap for Semiconductors¹ for applications such as CMOS (complementary metal oxide semiconductor) gate dielectrics and MIM (metal-insulator-metal) capacitors. On the one hand, integration of MIM structure for the next generation of radio frequency chips is needed. Increasing the dielectric constant of the dielectric used in MIM structures allows an increase of the capacitance density. In addition to a high dielectric constant, the material must satisfy a large number of requirements different to CMOS gate oxide specifications such as a high degree of capacitance linearity, a high dielectric breakdown ($E_{bd} > 5$ MV cm⁻¹), and a low thermal budget (<450 °C) specific to back-end processes. Efforts were first engaged to obtain MIM structures using Ta₂O₅. However, large leakage current has been observed²⁻⁴

and MIM capacitors are tested rather with “medium κ ” [such as HfO₂,⁵ Al₂O₃,⁶ and Y₂O₃⁷ or with “very high κ ” dielectrics (such as SrTiO₃ or BaTiO₃). On the other hand, the aggressive scaling of CMOS devices beyond the 0.1 μ m generation is driving the SiO₂ gate dielectrics to its physical limits, due to excessive direct tunneling leakage current. High dielectric constant (high-k) materials are attracting candidates for SiO₂ replacement. Indeed, they allow an increase of the physical thickness of the dielectric layer in the device while preserving the capacitance value.⁸ Most high-k studied materials are based on metal oxides (MO_x) and their silicates (M_xSi_yO_z). For instance, currently several dielectric materials such as Al₂O₃, ZrO₂, and HfO₂, as well as mixed oxides containing SiO₂ (silicates) or Al₂O₃ (aluminates) are being studied extensively. Y₂O₃ and rare earth oxides such as La₂O₃, Pr₂O₃, and Gd₂O₃ are also proposed as good candidates to replace SiO₂ thanks to their reasonably high permittivity ($10 < \kappa < 30$), compatibility when in direct contact with Si,⁹ good thermal stability, and relatively large conduc-

^{a)}Electronic mail: cdurand@cea.fr

tion band offset (2.3 eV for Y_2O_3).¹⁰ Although previous studies have revealed that these oxide films absorb water^{11–13} and present significant charge density responsible for deteriorated electrical characteristics, interesting results have been found on Y_2O_3 and Y-based silicate. For instance, Chambers and Parsons pointed out that yttrium has a very high affinity for oxygen and showed that an annealing results in the thickness reduction of SiO_2 to form a silicate layer.^{14,15} Copel *et al.* take advantage of the high stability of Y-O bondings to accurately control the silicate formation by developing a solid-state technique: the unwanted interfacial SiO_2 is consumed by yttrium oxide to form a silicate layer, which seems to be thermodynamically favorable.^{16,17} In spite of a lower permittivity than metal oxides, silicates are expected to have beneficial properties with lower charge densities compared to metal oxides thanks to similarities with SiO_2 . To avoid interfacial reaction, the high-k layer can be capped to protect the film from water ambient absorption (OH species favor the interface formation), as proposed by Stemmer *et al.*,¹⁸ or a prenitrided sample can also be used to prevent Si diffusion from the substrate to form a silicate.¹⁵

Concerning deposition methods, physical vapor deposition (PVD) processes were traditionally used to deposit metal oxides. Y_2O_3 has been deposited by sputtering,^{19–22} by ionized cluster beam deposition,^{23–25} by ion beam sputtering,^{26–28} by pulsed laser deposition,²⁹ by electron beam evaporation,^{30–33} and by molecular beam epitaxy.^{34,35} However, most of PVD techniques may not be suited in large scale CMOS processing on 200 or 300 mm Si wafers. Sputtering processes may not be suitable because of possible electrical damages induced in the extremely sensitive channel region of CMOS devices. Chemical vapor deposition (CVD) methods are usually preferred. However, a key point of CVD processes (named MOCVD when precursors are metal-organic compounds) deals with how to provide a stable and reproducible precursor supply to ensure a perfectly controlled growth of thin metal-oxide films. The use of a pulsed-liquid-injection source has been proposed to overcome this difficulty.^{36–39} The use of plasma assistance has been also reported for MOCVD process on HfO_2 ,^{40,41} ZrO_2 ,⁴² Y_2O_3 ,⁴³ Hf, or Zr-based silicate⁴⁴ and for atomic layer deposition (ALD) process on ZrO_2 ^{45,46} and SrTiO_3 .⁴⁷ Even if processes using plasma assistance are not well understood and optimized in terms of parameter adjustments, it looks very attractive. For instance, Kim *et al.* showed that the oxygen plasma use in an ALD process improved ZrO_2 film quality with a low carbon incorporation, a low leakage current, and negligible hysteresis compared to films deposited by conventional ALD.⁴⁶ Niu *et al.* achieved deposited yttrium oxide with oxygen plasma assistance and showed the presence of a three-layer structure Y_2O_3 /silicate/ SiO_2 after annealing at 900°C under N_2 .⁴³ Advantages of plasma assistance are, first, a decrease of the deposition temperature for low thermal budget applications as MIM capacitors and, second, a possible use of plasma effects as predeposition or postdeposition treatments.

In this paper, we investigate the formation of yttrium oxide and yttrium silicate films by plasma-enhanced MOCVD (PE-MOCVD) using a pulsed-liquid-injection

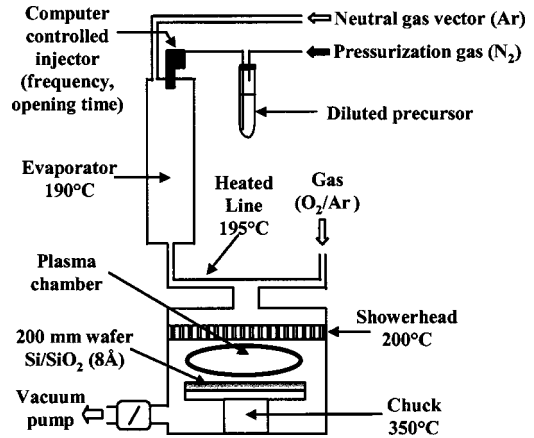


FIG. 1. Schematic of the PE-MOCVD experimental setup used to deposit yttrium oxide with the pulsed liquid-injection precursor source connected to the plasma chamber.

source. This type of source is hooked up to a plasma assisted MOCVD chamber. The role of plasma is to enable a lowering of the deposition temperature, which is particularly interesting for the deposition of dielectric films compatible with back-end thermal budget constraints (<450°C). We will indeed show that yttrium oxide deposition at below 380°C can be performed. The films chemical structure is analyzed by x-ray photoelectron spectroscopy (XPS) and by Fourier-transform infrared spectroscopy (FTIR) in the transmission mode. X-ray diffraction (XRD) is also used for the study of thick crystallized films. Results on thick (~40 nm) and ultrathin (~4 nm) films are presented. The interface nature and formation are analyzed and the influence of deposition parameters such as the reactive species incoming frequency is discussed. It is shown that the injection frequency plays an important role in the formation of the silicate and of the interfacial layer. The role of temperature is also investigated. Finally, electrical results are shown for as-deposited and annealed films.

II. EXPERIMENTAL PROCEDURE

A. The deposition process

Yttrium oxide films were grown by pulsed-injection plasma-assisted MOCVD. The experimental setup is shown in Fig. 1. The gas phase is generated using a pulsed-liquid-injection source. The liquid precursor is maintained at room temperature in a closed vessel pressurized under an inert gas (N_2 at 2 bars). The liquid reservoir is connected to a high-speed electrovalve (a car injector) driven by an electrical pulse, which is controlled by computer. Microamounts of liquid solution are injected into an evaporator held at 190°C and are “flash” evaporated. The precise amount of reactive species in the reactor is controlled accurately by the injection opening time and injection frequency. With this innovative delivery scheme, reasonable vapor pressures of thermally unstable precursors can be obtained and kept stable over the deposition run and thus complex oxides can be reproducibly grown.^{37,39} For the time, this delivery scheme was combined, in this study, to a plasma-assisted CVD chamber. The plasma is driven by a 380 kHz power supply and pressure in the

TABLE I. The standard process conditions of the plasma chamber and of the pulsed-liquid precursor source, respectively.

Standard plasma chamber parameters	Pressure	Gas	Input plasma power	Wafer temperature
	0.27 kPa (2 Torr)	O ₂ 250 SCCM	70 W	350 °C
Standard injection parameters	Dilution	Injection number	Frequency	Opening time
	0.02 mol/l	1–5000	1–10 Hz	2 ms

chamber can be adjusted between 27 and 670 Pa (0.2 and 5 Torr). A showerhead ensures a uniform distribution of gas stream over the heated wafer substrate (resistive heating).

For the present study, tri(2,2,6,6-tetramethyl-3,5-heptanedionate) yttrium [abbreviated as Y(tmhd)₃] was used as a precursor. The metal-organic precursor, which is a solid powder, was dissolved in a solvent (cyclohexane). The gaseous reactive species in the evaporator were transferred via a heated line (195 °C) to the reaction chamber using a neutral carrier gas [Ar at 30 SCCM (SCCM denotes cubic centimeter per minute at STP)]. The plasma gases were formed from Ar and O₂. The reaction chamber was maintained at low pressure, typically 0.27 kPa (2 Torr). The films were deposited on p-type 8 in. Si(100) substrates with 0.8 nm thermally grown SiO₂. The standard deposition conditions are given in Table I. Postdeposition annealing were performed on selected samples to investigate their electrical properties.

B. Characterization techniques

XPS, FTIR, and XRD were used to identify the bulk as well as the interface chemistry and structure of the films. The XPS spectra were collected with an Al K α x-ray source ($h\nu=1486.6$ eV) and an electron energy analyzer operating in a constant pass energy mode (50 and 20 eV for the survey and core level spectra, respectively). All studies were done at 45° as takeoff angle except for the angle-resolved studies. Spectral deconvolution was performed to extract the Si 2p, O 1s, C 1s, and Y 3d peak intensities. Chemical compositions were derived from the areas of the different XPS spectra weighted by corresponding sensitivity factors available from the database of the acquisition software. To check the XPS quantification, both XPS and RBS (Rutherford backscattering spectroscopy) were done on an Y₂O₃ layer, which was elaborated on silicon by thermal MOCVD at 700 °C. The [O]/[Y] ratio was found identical in RBS and XPS analyses using the Y 3d and O 1s sensitivity factors from XPS database. For the interfacial oxide thickness, we used a SiO₂ escape depth model from Si 2p spectra. Si 2p spectra were fitted with a Shirley background and five chemical states (Si⁰, Si¹⁺, Si²⁺, Si³⁺, Si⁴⁺), which are separated by approximately 1 eV each, with an increasing FWHM (the full width at half maximum). The fitting peak characteristics are presented in Table II. The peak from the substrate is located at 99.3 eV and is denoted Si⁰. The interfacial layer thickness of oxidized silicon t_{ox} is usually calculated using Eq. (1),⁴⁸

TABLE II. Binding energy, FWHM (full width at half maximum) and peak shape (Lorentzian-Gaussian percentage) for each Si oxidation state to fit the Si 2p XPS region.

Oxidation state	Binding energy (eV)	FWHM	Lorentzian (L) Gaussian (G) percentage (%) (L:100 and G:0)
Si ⁰	99.3	0.9	25
Si ¹⁺	100.3	1.0	0
Si ²⁺	101.1	1.2	0
Si ³⁺	102.1–102.3 ^a	1.3–1.5 ^a	0
Si ⁴⁺	103.3	1.4	0

^aVariable values, which depend on fitting results.

$$t_{ox} = \lambda_{ox} \sin(\theta) \ln\left(\frac{R}{R^\infty} + 1\right), \quad (1)$$

where θ is the photoelectron takeoff angle, R is the ratio A_{ox}/A_{Si} of the sample (A_{Si} being the relative areas of the Si⁰ component and A_{ox} the sum of the relative area of the Siⁿ⁺ components), R^∞ is the ratio A_{ox}/A_{Si} in the case of a thick thermal SiO₂ and bulk Si sample. The photoelectron inelastic mean-free path λ_{ox} is difficult to estimate for our interface. Nevertheless, the ratio R evolution gives a good qualitative image of the interface thickness because λ_{ox} , θ , and R^∞ can be considered constant. Therefore, the ratio R will be used to describe the oxidized Si-based compounds' thickness evolution. High-k compounds are insulating, which leads to charging effects as evidenced by a shift to higher binding energies of XPS peak positions. This effect has been systematically corrected by positioning, when detectable, the Si 2p peak from the substrate at 99.3 eV. This correction leads to C 1s peak position from surface contamination at 285.7 eV. When no Si 2p contribution from the substrate could be detected by XPS, the charging correction was carried out relative to this surface C 1s peak position. The samples' surfaces were treated by an Ar⁺ ion beam (1.5 keV @ 10 μ A during 30 s) only for thick layers before XPS analysis to remove the organic surface contamination. We initially determined Y₂O₃ peak positions with a ceramic Y₂O₃ sample (sintered Y₂O₃ powder annealed at 1500 °C during 24 h). The Y 3d_{(3/2)-(5/2)} doublet is located at 156.7 and 158.7 eV in agreement with literature data on Y₂O₃ reference compounds.⁴⁹ Also, the solid precursor powder of Y(tmhd)₃ was analyzed by XPS with a monochromatic source at 35° takeoff angle in order to locate the Y energy binding in the precursor molecule environment. A study of the bonding environments in the grown material and at the interface was also carried out using FTIR. A Bruker IFS 55 Fourier-transform infrared spectrometer was used. The resolution and number of scans were set at 4 cm⁻¹ and 500, respectively. Capacitance-voltage (C-V) and current-voltage (I-V) measurements were conducted on a HP 4284 A precision LCR meter and HP 4156 A meter, respectively. The structure was metal-oxide semiconductor formed by evaporating gold on the films through shadow masks. Four different surfaces (0.354×10^{-2} , 0.694×10^{-2} , 1.71×10^{-2} , 2.78×10^{-2} mm²) were defined. The equiva-

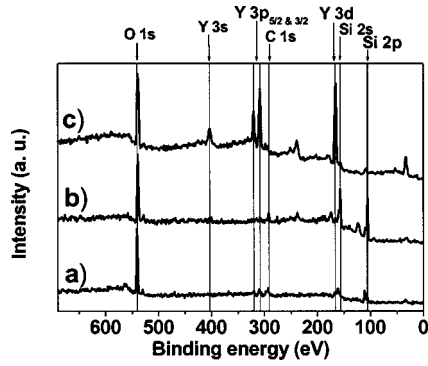


FIG. 2. XPS survey scans for (a) process with only plasma enhanced at 70 W (as PECVD), (b) process with only substrate heating at 350°C (as MOCVD), and (c) process with both plasma and substrate heating at 70 W and 350°C, respectively (PE-MOCVD). This graph shows the synergy between the plasma and the substrate heating to deposit Y_2O_3 layers using the PE-MOCVD technique.

lent oxide thickness (EOT) was extracted from the accumulation region (no quantum mechanical correction was applied).

III. RESULTS AND DISCUSSION

A. Plasma enhanced MOCVD: Plasma effects

In order to work out the influence of the plasma and of the substrate temperature on the process, we performed three different experiments: (a) deposition using plasma assistance (70 W) but without heating the substrate, (b) deposition at 350°C without plasma, and finally (c) deposition using both thermal (350°C) and plasma assistance (70 W). The XPS analyses of the three samples are shown in Fig. 2. As expected, there is no deposited yttrium for the run performed without heating the substrate chuck (the actual substrate temperature is estimated to be lower than 150°C) [Fig. 2(a)]. At 350°C, when no plasma is used, yttrium is not detected as well [Fig. 2(b)]. Clearly the plasma is needed to form an yttrium oxide film from the β -diketonate $\text{Y}(\text{tmhd})_3$ precursor at such a low temperature [Fig. 2(c)]. Indeed, the Y 3d, 3p, and 3s signatures are only observed in this case. A study of several key parameters (pressure, O_2 partial pressure and flux, plasma power) was carried out to understand deposition mechanisms and to optimize the process. Apparently, the plasma promotes the precursor decomposition but also induces two other opposite effects: (i) carbon deposition from the solvent and from the precursor organic chains dissociation and (ii) carbon etching. For several sets of deposition conditions, we determined threshold values beyond which a thick carbon layer is deposited instead of yttrium oxide. When the plasma density is high, it strongly decomposes carbon chains from the solvent and the precursor. If the O_2 partial pressure is too low, all carbon groups on the substrate surface cannot be etched and thus carbon species are incorporated during the growth. The use of oxygen in the plasma gas phase ensures minimum carbon contamination and oxygen stoichiometric adjustment of the deposited layer. However, a too high oxygen partial pressure in the plasma and a too high plasma power can also lead to an undue increase of deleterious SiO_2 at the interface. Therefore, optimization of

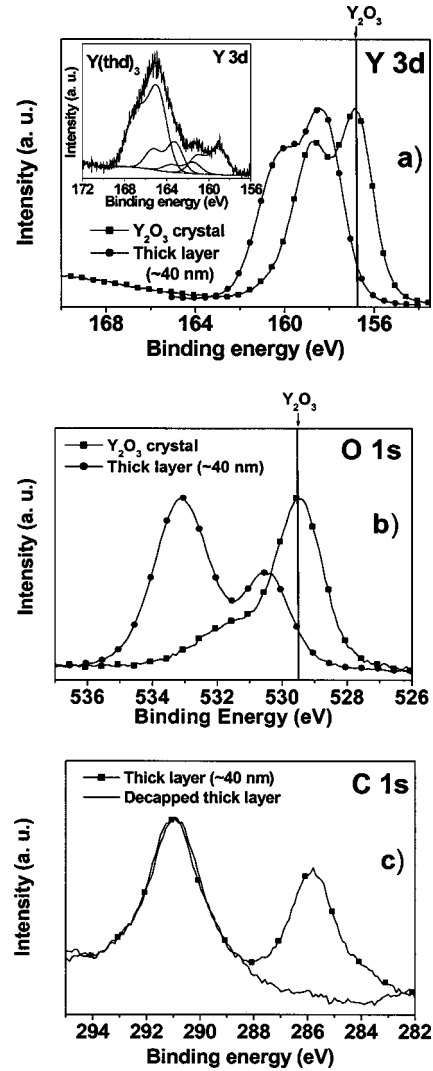


FIG. 3. XPS analysis [(a) Y 3d, (b) O 1s, and (c) C 1s regions] for a thick yttrium oxide layer (~40 nm) processed in the standard deposition conditions. Spectrum of an Y_2O_3 crystal is also presented for comparison on Y 3d and O 1s regions. Furthermore, Y 3d region of the precursor $\text{Y}(\text{tmhd})_3$ powder analysis is inserted. The C 1s region is presented before and after surface sputtering.

the deposition conditions should take these different points into account (Table I). The plasma power was fixed to 70 W in order to limit the solvent decomposition and wafer oxidation. The working pressure was fixed at 0.27 kPa (2 Torr) in order to maintain a reasonable thermal exchange for the substrate heating, while, at the same time, to decrease energetic ion bombardment at the surface of the growing film, which may induce a high interfacial state density. Indeed, the plasma is localized near the showerhead and the sheaths are collisional. In this case, the plasma is similar to a “remote plasma.”

B. Properties of thick yttrium oxide films

Figure 3 presents the Y 3d, O 1s, and C 1s XPS spectra for a thick (~40 nm) film deposited in the standard condition (Table I) using an injection frequency of 5 Hz. The corresponding Y 3d and O 1s spectra for an yttrium oxide reference ceramic are also shown, after surface sputtering. In

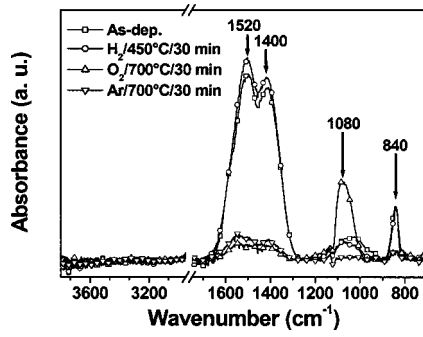


FIG. 4. The graph shows FTIR spectra for the thick sample and three annealing post-treatments. The as-deposited film is denoted by curve with squares (■), the H₂ annealed at 450°C for 30 min by the curves with circles (●), the O₂ annealed at 700°C for 30 min by the curves with up triangles (▲), and finally the Ar annealed at 700°C for 30 min by curves with down triangles (▼).

the reference material, the Y 3d_{5/2-3/2} doublet position (respectively, 156.7 and 158.7 eV) and O 1s peak (529.5 eV) are consistent with literature data for Y₂O₃. The peak shoulder around 531.8 eV has also been observed by several authors and has been attributed to O-H bonding¹⁴ or oxygen trapping.²⁹ Before sputtering the reference ceramic, this peak was higher relatively to the main one at 529.5 eV, indicating that surface bonds are involved. For the PE-MOCVD film grown at 350°C, the Y 3d_{(5/2)-(3/2)} doublet is located at 158.5–160.5 eV [Fig. 3(a)]. This could correspond to Y-O-Si bonds, however, as we do not observe any peak in the Si 2p region, it is attributed to Y-O-C bonding and H contamination. The Y-O-H bond has already been reported to explain the shifted Y 3d doublet.⁵⁰ However, in our case, FTIR analysis (Fig. 4) does not show any O-H signature (3000–3700 cm⁻¹). The carbon bonding to oxygen is expected to shift the Y 3d peak toward higher binding energies as compared to Y-O binding in Y₂O₃ by considering the electronegativity of carbon. The shift of Y-O-C bonding should also be larger than for Y-O-Si because C has a higher electronegativity compared to the Si one (respectively, 2.5 and 1.8 eV). For the organic precursor Y(tmhd)₃, the shift is indeed quite important as yttrium is bonded to three tmhd ligands as shown in the insert of the Y 3d region, Fig. 3(a) (165.0 eV for the main component, the smaller one probably correspond to additional yttrium bindings due to air exposure). If a constant splitting of 2.0 eV is assumed for the Y 3d doublet, the fitting of the Y 3d spectrum requires at least two components for each peak, which indicates a multiple yttrium bonding environment (C and H presumably). Consistent with this, the O 1s peak at 530.6 eV can be attributed to Y-O-C bonds with H contamination [Fig. 3(b)]. The second peak at 533.0 eV comes from O-C bonds in the deposited layer and also from organic surface contamination. Indeed, after sputtering the surface, this peak decreases to the same level as the 530.6 eV one. The C 1s region [Fig. 3(c)] exhibits two distinct contributions located, respectively, at 285.7 and 291 eV. The first one comes only from organic surface contamination, because this peak disappears after sputtering the surface. On the contrary, the second peak corresponds to carbon in the film. As a conclusion, the thick films grown at 350°C using an injection frequency of 5 Hz

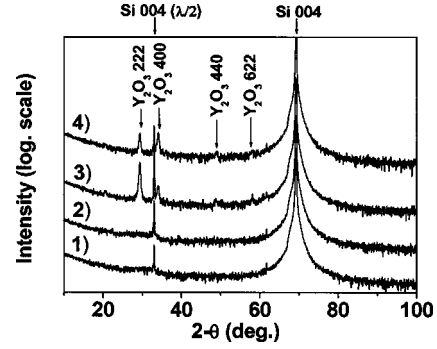


FIG. 5. XRD diagrams for (1) as-deposited sample, (2) H₂ annealed at 450°C, (3) Ar annealed at 700°C, and (4) O₂ annealed at 700°C.

contain Y-O bonds with no indication of silicate-type bonds but rather C and H environments. Incorporation of organic residue in the film is likely to occur during deposition at low temperature due to incomplete decomposition of the precursor. This is confirmed by the FTIR spectrum (Fig. 4) that shows a band at 840 cm⁻¹ and two other broad bands centered on 1520 and 1400 cm⁻¹. These bands are assigned to C-O and C-H stretching modes.

The previous film was annealed under Ar or O₂ flow at 700°C or under H₂ flow at 450°C for 30 min. The $\theta/2\theta$ x-ray diffraction diagrams (Fig. 5) indicate crystallization of the film at 700°C, whereas it is still amorphous (or nanocrystallized) at 450°C. XPS spectra are shown in Fig. 6 (after Ar sputtering). The formation of Y₂O₃ upon Ar or O₂ annealing at 700°C is confirmed by the Y 3d and O 1s peaks' positions [Figs. 6(a) and 6(b)]. The Y 3d_{5/2} peak is located at 156.7 eV with a lower FWHM corresponding to Y-O bonds in an Y₂O₃ crystal. Likewise, the O 1s peak at lower binding energy becomes the main contribution and is

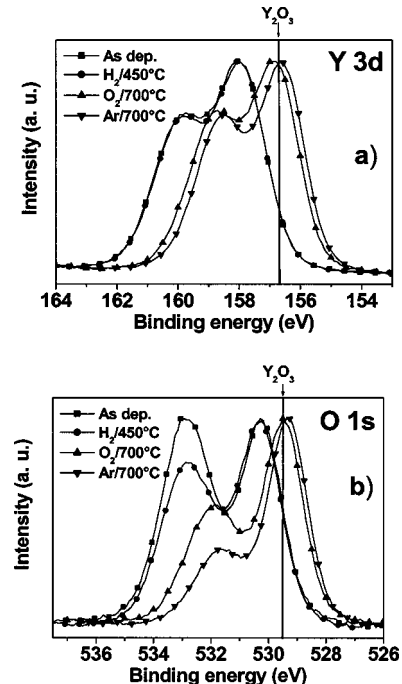


FIG. 6. XPS spectra [(a) Y 3d and (b) O 1s regions] for as-deposited thick sample and three annealing post-treatments after Ar sputtering for surface contamination removal (same symbols as in Fig. 4).

shifted to 529.5 eV as in Y_2O_3 crystal. Moreover, the 700 °C annealings reduce the C impurities in the layer, since the intensity of broadbands around 1520 and 1400 cm^{-1} and band at 840 cm^{-1} are considerably attenuated on the FTIR spectra (Fig. 4). This effect is also visible with XPS analysis on the O 1s region [Fig. 6(b)] where the contribution attributed to O-C bonds (at 533 eV) is reduced compared to O-Y peak near 530 eV. We note on FTIR spectra a significant increase of the peak at 1080 cm^{-1} corresponding to transversal optical mode of Si-O bond in silicon dioxide for 700 °C O_2 annealing. To conclude, a high temperature annealing leads to the crystallization of the as-deposited films and to a decrease in carbon content.

C. Analysis of thin films: Effects of injection frequency on the interface layer and silicate formation

1. XPS analysis

By varying the injection frequency (from 1 up to 10 Hz), we intended to vary the reactive species supply rate at the substrate surface, which might influence the interface layer growth. The standard conditions were used for all other parameters (Table I). For each experiment, the injected volume was the same (1000 injections), which corresponds to a layer thickness thin enough (<10 nm) to detect the silicon substrate by XPS, except for the 10 Hz film. The thickness was found to increase with increasing injection frequency. XPS was used to study both the film and the interface (no Ar sputtering was used prior to measurements in order to prevent film or interface degradation). Figure 7 presents the Si 2p, Y 3d, and O 1s XPS regions of layers grown at increasing injection frequency. The Si 2p spectra [Fig. 7(a)] are normalized to the Si^0 peak area (the substrate peak Si^0 is at 99.3 eV). If not normalized, the Si^0 peak decreases with increasing injection frequency, indicating an increase of the film thickness. A bare SiO_2 (0.8 nm)/Si substrate is also shown for comparison. The corresponding Si-O peak is located at 103.3 eV, which is the expected binding energy for SiO_2 . Clearly from Fig. 7(a), the Si-O peak for the different films is shifted towards lower energies than the binding energy of SiO_2 , which can be assigned to Y-O-Si type of bonds. The expected range of Si 2p in Y-O-Si binding is indeed in the 101.5–103 eV range, depending on the exact silicate composition.⁵¹ Also the FWHM of the Si-O Si 2p peak, which is of 1.6 eV for SiO_2 in the bare substrate, is strongly increased for the films (to 2.2 eV), which indicates a wide range of Si-O bonding in the films. Finally, the normalization to the silicon substrate Si 2p peak area clearly emphasizes the increasing content of silicate-based compounds in the films with decreasing injection frequency. This point will be specified later (Sec. III C 2). In the Y 3d region [Fig. 7(b)], the Y 3d_{5/2} and Y 3d_{3/2} peaks are located at, respectively, 158.7 and 160.7 eV for the 1 Hz film. These positions are coherent with Y-O-Si bonds, which have been evidenced also on the Si 2p region. However, Y-O-C bindings cannot be precluded at this point as we showed that the corresponding Y 3d doublet appears for similar energies [Fig. 3(a)]. The Y 3d splitting is progressively less pronounced with increasing injection frequency (whereas its lo-

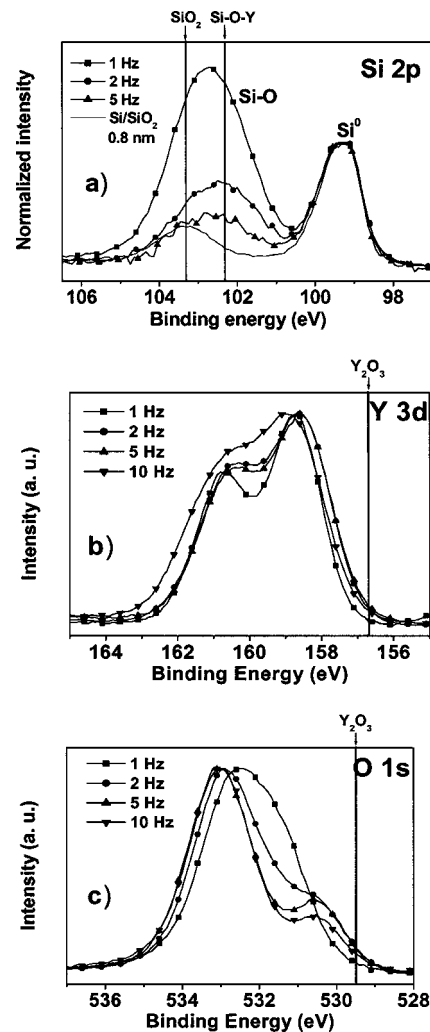


FIG. 7. XPS spectra [(a) Si 2p, (b) Y 3d, and (c) O 1s regions] for samples with increasing injection frequency [1 Hz (●), 2 Hz (•), 5 Hz (▲), and 10 Hz (▼)]. Si 2p spectra are normalized on Si^0 peak area (peak from substrate) in order to estimate the oxidized Si-based compound thickness, since the well-known method for measuring the thickness of oxide film by XPS is based on the area ratio between the oxidized silicon $\text{A}^{\text{Si-O}}$ and substrate silicon A^{Si} . The spectrum of initial substrate [Si/SiO_2 (0.8 nm)] is also done for comparison.

cation is only slightly changed), indicating a much wider Y-O bonding environment, probably arising from both Y-O-Si and Y-O-C type of bonds. On the other hand, the 1 Hz sample consists of a well-defined bonding (presumably a silicate compound with no secondary yttrium carbonate phase as shown hereafter in the following section). No evidence for Y-Si bonds from silicides was found on the Y 3d or Si 2p regions (expected at ~ 156.5 and 98.7 eV, respectively). On the O 1s region [Fig. 7(c)], the peak shape also changes progressively with the injection frequency. For high frequencies (5 or 10 Hz), two separated peaks appear. One is at 533 eV (FWHM=2.0 eV), which corresponds to the binding energy in SiO_2 and, as we showed it previously [Fig. 3(b)] to the binding energy in O-C chains of organic residues and surface contamination. The second peak at 530.6 eV is attributed to Y-O-C and also to Y-O-Si bindings. For the 1 Hz sample, a broad peak is observed. The significant peak

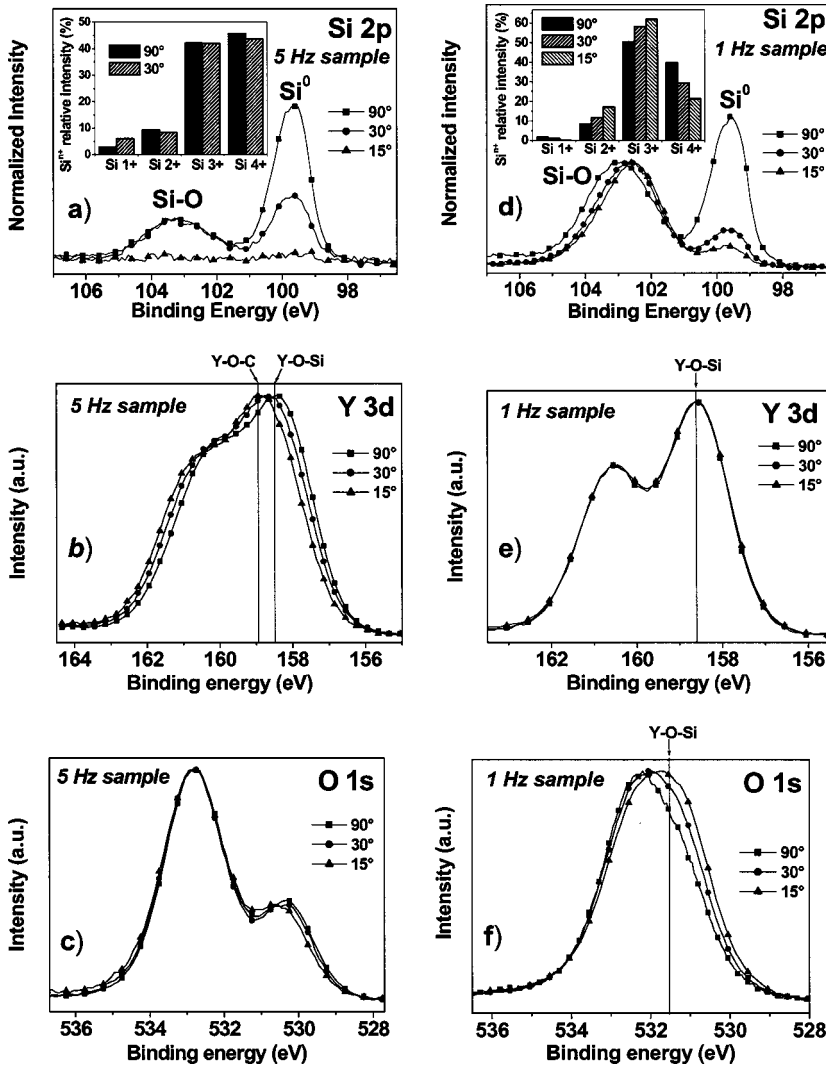


FIG. 8. Angle-resolved XPS analyses (Si 2p, Y 3d, and O 1s regions) at three takeoff angles [90° (■), 30° (●) and 15° (▲)] of the 5 Hz sample [(a), (b), and (c)] and the 1 Hz sample [(d), (e), and (f)]. Note that the intensity of Si 2p spectra is normalized on the Si-O peak. The relative intensity of each Siⁿ⁺ contribution for the different takeoff angle analyses extracted from the Si 2p fit model is plot in the insert of Si 2p regions [(a) and (d) corresponding to the 5 and 1 Hz samples, respectively].

contribution around 531.5 eV is consistent with a silicate compound¹⁴ and confirms the observation made on the Y 3d and Si 2p regions.

2. Angle-resolved XPS analysis

In order to get some insight on the nature and chemical structure of both the interface (in contact with the silicon substrate) and film, we performed angle-resolved XPS (AR-XPS) on the 1 and 5 Hz films. Three different takeoff angles were studied (90° and two grazing incidence angles: 30° and 15°). Note that, when the takeoff angle decreases, the probed depth decreases as well, so that surface contributions are enhanced. Figure 8 shows the Si 2p, Y 3d, and O 1s XPS regions for both samples. The Si 2p spectra intensity is normalized on the Si-O peak area. Thus, the substrate Si⁰ peak clearly decreases with decreasing takeoff angle as expected (for the 5 Hz sample, the substrate is even not probed at 15°). A quantitative analysis of the Si-O Si 2p peak was carried out by considering four Si oxidized states (Si¹⁺, Si²⁺, Si³⁺, and Si⁴⁺, see Table II). The result of the fitting procedure is given in the inserts on the Si 2p regions [Figs. 8(a) and 8(b)] by a relative intensities bar graph of each Siⁿ⁺ (n=1–4) contribution. The Si³⁺ contribution is shifted by 2.8–3.0 eV compared to Si⁰. This value is larger

than the common value reported for the Si³⁺ suboxide (2.6 eV) in a conventional SiO₂/Si interface.⁵² The fitting using a imposed 2.6 eV shift position value for the Si³⁺ component was clearly not adapted. The presence of such a component of oxidized Si, abnormally shifted relative to Si³⁺ in Si/SiO₂, is attributed mainly to silicate-type bondings Si-O-Y (this does not mean that we exclude the presence of substoichiometric SiO_x, but the corresponding contribution is overlapped by the silicate one due to our limited energy resolution). Other reasons support the Si³⁺ assignment to mainly silicate bonds. First, the Y 3d peak position at 158.7 eV is consistent with silicate Y-O-Si bonds. Second, the Si³⁺ intensity from substoichiometric SiO_x compared to the other oxidized contributions (i.e., Si¹⁺, Si²⁺, and Si⁴⁺) is limited, since it represents only 11.3% of the Si-O signal for the initial SiO₂(8 Å)/Si substrate. Even when the initial substrate is exposed under O₂ plasma during 1500 s (under the standard plasma chamber parameters presented in Table I) without injection, an increase of contribution from substoichiometric SiO_x (i.e., Si¹⁺, Si²⁺, and Si³⁺) is not observed and the Si³⁺ peak represents 8.2% of the Si-O signal. On the contrary, when the yttrium precursor is injected, the Si³⁺ is strongly enhanced, since the Si³⁺ signal represents 46.5% and 39.8% of the Si-O peak on the 5 and 1 Hz sample,

respectively. Such an increase is likely to arise mainly from a silicate contribution. Electron energy-loss spectroscopy measurements have been done and confirmed the presence of silicate (not shown here). It is worth noting that a similar fitting procedure was employed to study $\text{Al}_2\text{O}_3/\text{Si}$ interface in Ref. 53. As the deposited film is amorphous, silicate-type bindings is most likely in multiple bonding environment. Therefore, a part of the Si^{2+} contribution is certainly assigned to silicate-type bondings. As the O_2 plasma under the standard conditions is not energetic, the incompletely oxidized silicate presence is a reasonable hypothesis.

For the 5 Hz sample, no shift of the Si-O peak is observed when the incidence angle changes from 90° to 30° . No significant change is also observed in the relative intensity of the Si^{3+} and Si^{4+} contributions between 90° and 30° [insert of Fig. 8(a)]. Hence, the 5 Hz film is composed of an yttrium silicate, which is probably present at the interface (or on top of a very thin SiO_2 layer that cannot be resolved by changing the takeoff angle). Since the Si 2p peak disappears at 30° , no silicon atom is present at the top surface. Thus, the silicate film does not extend up to the top surface and the top layer consists of $\text{Y}_x\text{O}_y\text{C}_z$ film. Indeed, the Y 3d angle-resolved peak exhibits a slight shift towards higher energies (+0.5 eV from 158.5 to 159.0 eV) with decreasing takeoff angle that corresponds to an Y-carbonate signature enhancement compared to the Y-silicate signal, since at 15° no silicate is involved in the measured response (accordingly to the Si 2p region). These observations are consistent with the presence of two kinds of bindings distributed differently in the sample: Y-O-C (top surface) and Y-O-Si (interface). As we already mentioned it for the thick sample analysis (Fig. 3), the binding energies of Y-O-Si and Y-O-C are quite close. The peak located at 532.8 eV, which does not shift with decreasing angle, indicates that the C contamination is uniformly distributed in the film.

For the 1 Hz sample, the Si-O peak from the Si 2p region is significantly shifted (-0.5 eV) towards lower binding energies for decreasing takeoff angle, which clearly indicates a distribution of different silicon-oxide based compounds within the depth of the film. The quantitative analysis [insert of Fig. 8(d)] shows a strong increase of silicate signals (Si^{2+} and Si^{3+}) and a clear decrease of the SiO_2 contribution (Si^{4+}) at grazing angles. The sample appears composed of a SiO_2 interface with the silicon substrate and of a silicate layer on top of it. The increasing contribution at 531.5 eV [Fig. 8(f)] with decreasing takeoff angle is consistent with this picture. Since no shift is observed on the Y 3d peak [Fig. 8(e)], there is no $\text{Y}_x\text{O}_y\text{C}_z$ layer.

These characterizations lead us to propose two different microstructures for the 1 and 5 Hz films, which are depicted in Fig. 9. At low injection frequency (1 Hz), the film is composed of an yttrium silicate layer with an interfacial SiO_2 layer in contact with silicon (Si/SiO_2 (~ 4 nm)/ $\text{Si}_x\text{O}_y\text{Y}_z$). At higher frequencies, the interfacial layer is rather an yttrium silicate (silicon rich) with an yttrium oxide layer on top of it with carbon impurities ($\text{Si}/\text{Si}_x\text{O}_y\text{Y}_z$ (~ 2 nm)/ $\text{Y}_x\text{O}_y\text{C}_z$). This picture was confirmed by transmission electron microscopy

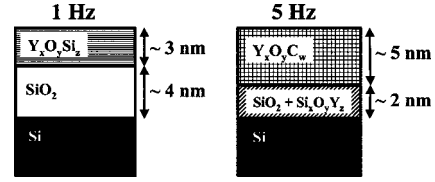
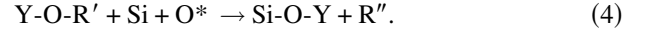
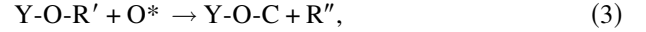


FIG. 9. Diagram illustrating the difference between the 5 and 1 Hz structure consistent with AR-XPS.

and electron energy-loss spectroscopy investigations. However, if the 1 Hz sample is grown thicker (~ 40 nm), a top $\text{Y}_x\text{O}_y\text{C}_z$ film is grown too.

3. Discussion

The injection frequency (i.e., the flux of reactive species) has a strong effect on the plasma density and composition, which may influence the growth mechanisms. We propose the schematic reactions (shown below) during the deposition. These reactions are inspired by those proposed by Niu *et al.*,⁴³



The reactions are written schematically, and are not balanced. Reaction (2) is the silicon oxidation by the energetic oxygen species (denoted O^*) from the oxygen plasma that is enhanced by volatile organic compounds, denoted R. Indeed, oxidation rate is strongly limited (0.03 nm/min) when experiments are carried out without injection under standard process conditions (Table I), whereas it is strongly increased when solvent (cyclohexane) is injected into the oxygen plasma (0.12 nm/min at 5 Hz).⁵⁴ Reaction (3) is the formation of yttrium oxide carbonate by decomposition and oxidation reaction of the organic $\text{Y}(\text{tmhd})_3$ precursor molecule thanks to the oxygen plasma. The precursor molecule is represented by $\text{Y-O-R}'$, where R' is the organic ligand [reactions (3) and (4)]. Only a schematic reaction is proposed here since decomposition paths of precursor molecules such as $\text{Y}(\text{tmhd})_3$ is far too complicated to be described and is not known in detail. R'' denotes compounds resulting from the precursor decomposition, i.e., the organic ligand R' itself and oxidation by-products of the organic ligand. Indeed, the analysis of the light emitted by plasma using optical emission spectroscopy (not shown here) indicates clearly the CO , CO_2 , and H_2O signatures in the plasma phase. Reaction (4) describes the silicate formation by decomposition of the precursor and reaction with Si, which is enhanced by the O_2 plasma. Silicate films can contain a slight carbon contamination. Reaction (2) and (4) occur at the substrate interface, whereas reaction (3) is the main deposition mechanism far from the interface. For a high reactant flow, i.e., at 5 Hz injection frequency, a high reactive species quantity is present on the substrate surface and reactions that consume precursor molecules are favored, i.e., reactions (3) and (4). The interface mainly results in silicate compounds, since re-

action (4) is enhanced compared to reaction (2). Since the deposition rate increasing frequency as found previously by XPS (because the precursor quantity on the surface is higher), the interface reaction (4) is rapidly stopped because Si atoms diffusion is limited due to the rapid formation of the YOC layer and reaction (3) that leads to the formation of yttrium oxide carbonates becomes the only deposition mechanism. On the contrary, at 1 Hz, i.e., with a low reactant flux, the growth rate is lower (because the precursor quantity on the surface is lower) and reaction (4) will occur for a longer time than during the 5 Hz process because here the YOC layer growth is slower and the Si diffusion is less limited. In this case, reactions that consume silicon near the interface are more likely to occur, i.e., reaction (2), which leads to the formation of a thick SiO_2 layer, and reaction (4), which gives a silicate layer (on top of SiO_2). Beyond a critical thickness, the deposited layer at 1 Hz will be yttrium oxide (with carbon contamination) without silicon (as found for 40 nm thick layers deposited at 1 Hz), since reaction (4) is limited by the presence of Si atoms. Beyond a critical distance from the substrate, no silicon is available and only reaction (3) occurs. From this study, it appears that a high reactive species flux should be preferred to limit the formation of the interfacial SiO_2 layer.

D. Effect of substrate temperature

Five different substrate temperatures (in the range 200–380°C) were investigated for films grown at 1 Hz in the standard conditions given in Table I. A same precursor liquid volume was injected (1000 injections). The films were investigated by XPS (no Ar sputtering was performed prior to measurements since the films were very thin (<10 nm)). Figure 10 shows the XPS spectra of the Si 2p, Y 3d, and O 1s lines (Si 2p spectra are normalized on Si^0). The XPS quantification from C 1s spectra (not shown here) shows that the C content increases with decreasing substrate temperature, as it is expected due to incomplete precursor decomposition. First, it appears that deposition can occur at temperature as low as 200°C. However, the sample grown at 200°C is significantly different with high carbon content with limited yttrium content (mainly in the form of Y-O-C and limited silicate). In the range 250–380°C, the Y 3d spectra are unchanged. The binding environment of Y is mainly Y-O-Si, as shown previously for the film grown at 350°C (158.8 eV). The O 1s and Si 2p regions indicate that the yttrium silicate thickness increases as compared to the SiO_2 one, when the deposition temperature increases (O 1s and Si 2p contributions around, respectively, ~ 531.5 and ~ 102.4 eV increase with increasing temperature). The quantitative analysis of the Si 2p region was done, as previously described (Table II), and the peak area of each Si^{n+} component ($n=1-4$), normalized to the Si^0 one, is plotted as a function of temperature in Fig. 11(a). The graph shows that the Si^{4+} ratio stays roughly constant, which indicates that the SiO_2 thickness is not significantly modified in the studied temperature range. On the contrary, the Si^{2+} and especially the Si^{3+} components increase with increasing temperature. These two contributions arise from a wide range of silicon

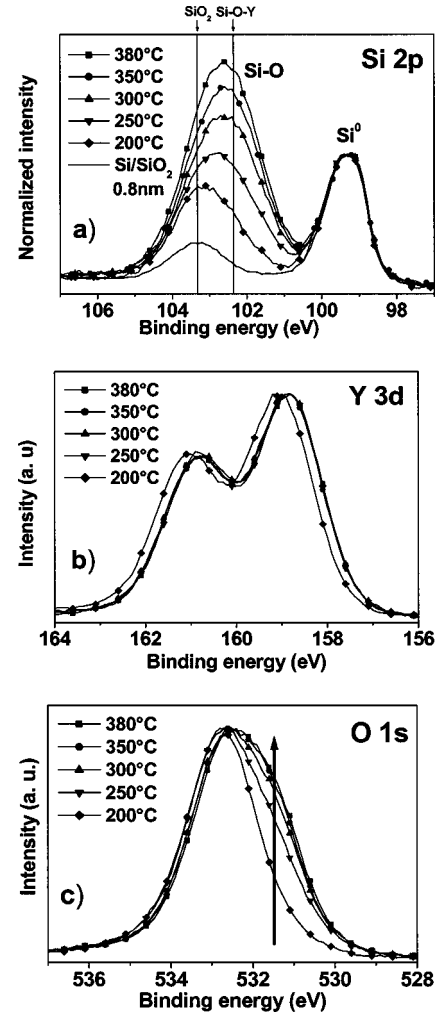


FIG. 10. XPS spectra [(a) Si 2p, (b) Y 3d, and (c) O 1s regions] for samples with increasing deposition temperature [380°C (■), 350°C (●), 300°C (▲), 250°C (▼), and 200°C (◇)]. As Fig. 7, Si 2p spectra are normalized on Si^0 peak area (peak from substrate) in order to estimate the oxidized Si-based compound thickness evolution. The spectrum of initial substrate [$\text{Si}/\text{SiO}_2(0.8 \text{ nm})$] is also done for comparison.

bonding environments available in Y-O-Si. Such an increase is related to the increase of the yttrium thickness with increasing temperature. In Fig. 11(b), the area ratio $A^{\text{Si-O}}/A^{\text{Si}}$ component ($A^{\text{Si-O}}$ is the sum of all area silicon oxidized components: Si^{1+} , Si^{2+} , Si^{3+} , and Si^{4+}) is represented in an Arrhenius-type plot, which shows the extent of the yttrium silicate thickness versus the inverse of the deposition temperature. The activation energy (E_a) for the silicate formation during deposition is equal to 12.5 kJ/mol. This value is rather low, which indicates that thermal activation is not significant in this temperature range, as could be expected (precursor's decomposition requires higher temperatures).

E. Electrical characterizations

A typical C-V curve measured with an electrode surface of $0.694 \times 10^{-2} \text{ mm}^2$ is shown in the insert of Fig. 12 for a film grown at 5 Hz ($\sim 40 \text{ nm}$). The EOT was extracted from the accumulation capacitance and is plotted in Fig. 12 for three film thicknesses (estimated by x-ray reflectometry). The intercept of the linear fit is equal to 1.7 nm ($\pm 1.3 \text{ nm}$).

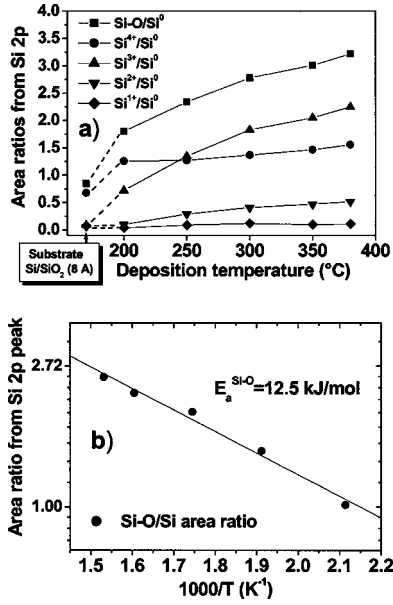


FIG. 11. Graph (a). Area ratios determined from the Si 2p fitting model vs the deposition temperature. The graph gives the area ratio Si-O/Si and also area ratio of each oxidation state. Graph (b). Arrhenius diagram of Si-O/Si area ratio vs $1000/T$. The activation energy is extracted from the slope.

The effective permittivity of the films extracted from the slope of the linear fit is of $7.5(\pm 1.2)$. This depressed value compared to Y_2O_3 is consistent with the presence of carbonate and silicate. Annealing of the thick films does not change significantly the EOT. For example, the EOT values extracted from the 1 kHz C-V measurements are 18.8, 17.2, 18.2 and, 16.9 nm for, respectively, as-deposited, 450°C H_2 annealed, Ar and O_2 700°C annealed samples. Although the 700°C thermal post-treatment significantly reduces the organic contamination and leads to the crystallization of the Y_2O_3 phase, the EOT value stays constant probably due to the increase of the interfacial layer. The current density measured as a function of applied voltage is plotted in Fig. 13 for a 40 nm thick film (grown at 5 Hz) and annealed samples. Electrical breakdown for the as-deposited film occurs at ~ 34 V (which corresponds to an electrical breakdown field E_{bd} of the order of 8 MV/cm) and the film exhibits a low leakage current density (below 10^{-7} A/cm² for a bias volt-

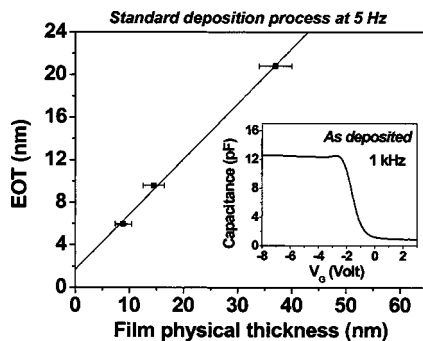


FIG. 12. EOT (equivalent oxide thickness) of films elaborated at 5 Hz using standard conditions (Table I) as a function of the film physical thickness estimated by x-ray reflectivity. The insert shows a C-V curve obtained for the ~ 40 nm yttrium oxide layer.

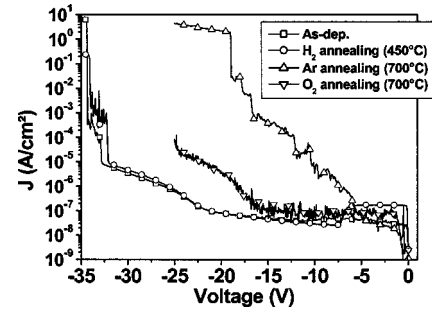


FIG. 13. Leakage current density vs voltage for thick Y_2O_3 film (~ 35 nm): as-deposited film (\blacksquare), 450°C annealed films under H_2 (\bullet), and 700°C annealed films under Ar (\blacktriangle) and O_2 (\blacktriangledown).

age ranging from -20 to 0 V). The dielectric breakdown field values are in good agreement with those expected from the relationship proposed by McPherson *et al.* that links E_{bd} and the dielectric constant κ [$E_{bd} \sim (\kappa)^{-1/2}$].⁵⁵ No significant change is observed on the $J(V)$ curve for the 450°C H_2 annealed film. The 700°C annealed films present a lower E_{bd} and a higher leakage current density, which are attributed to the film crystallization. To conclude, the as-deposited and 450°C-annealed films exhibit promising electrical properties, especially for MIM devices, which requires a low thermal budget.⁷

IV. CONCLUSION

Yttrium oxide and yttrium thin films were grown by pulsed-liquid-injection PE-MOCVD from $Y(tmhd)_3$ precursor. The plasma allows a significant reduction of the thermal budget as compared to conventional thermal MOCVD and yttrium silicate films can be grown at temperatures as low as 250°C. Depending on the incoming reactive species flow rate (which is tuned by the injection frequency), a SiO_2 or an yttrium silicate interface layer is favored. Beyond a critical thickness, yttrium oxide is formed but the low deposition temperature implies carbon contamination, which can, however, be reduced upon annealing at 700°C. The SiO_2 interfacial layer can be limited by increasing the injection frequency (i.e., at 5 Hz). Finally, the as-deposited films exhibit a high electrical breakdown field ($E_{bd}=8$ MV/cm) and a low leakage current density ($I < 10^{-7}$ A/cm²), which is a very promising result for MIM applications.

ACKNOWLEDGMENTS

The authors would like to thank warmly N. Rochat for helpful expertise on IR-analysis (FTIR), D. Muiard, G. Rolland, and M. Burdin for XRD analyses. F. Ducroquet is also thanked for helpful discussion on electrical characterizations. L. Vallier is also gratefully thanked for XPS expertise and deposition equipment support.

¹The International Technology Roadmap for Semiconductors, Semiconductors Industry Association, see also <http://public.itrs.net/> for the most recent updates.

²P. C. Joshi and N. W. Cole, J. Appl. Phys. **86**, 871 (1999).

³S. Blonkowski, M. Regache, and A. Halimaoui, J. Appl. Phys. **90**, 1501 (2001).

⁴T. Yoshitomi *et al.*, IEEE Bipolar/BiCMOS Circuits Tech. Meet. 1999, 133.

- ⁵H. Hu, C. Zhu, Y. F. Lu, M. F. Li, and B. J. Cho, IEEE Electron Device Lett. **23**, 514 (2002).
- ⁶S. B. Chen, C. H. Lai, and A. Chin, IEEE Electron Device Lett. **23**, 185 (2002).
- ⁷C. Durand *et al.*, J. Vac. Sci. Technol. A **22**, 655 (2004).
- ⁸G. D. Wilk, R. M. Wallace, and J. M. Anthony, J. Appl. Phys. **89**, 5243 (2001).
- ⁹K. J. Hubbard and D. G. Schlom, J. Mater. Res. **11**, 2757 (1996).
- ¹⁰J. Robertson, J. Vac. Sci. Technol. B **18**, 1785 (2000).
- ¹¹B. W. Busch, J. Kwo, M. Hong, J. P. Mannaerts, B. J. Sapjeta, W. H. Schulte, E. Garfunkel, and T. Gustafsson, Appl. Phys. Lett. **79**, 2447 (2001).
- ¹²T. Gongousi, M. Jason Kelly, and G. N. Parsons, Appl. Phys. Lett. **80**, 4419 (2002).
- ¹³D. Niu, R. W. Ashcraft, and G. N. Parsons, Appl. Phys. Lett. **80**, 3575 (2002).
- ¹⁴J. J. Chambers and G. N. Parsons, J. Appl. Phys. **90**, 918 (2001).
- ¹⁵J. J. Chambers and G. N. Parsons, Appl. Phys. Lett. **77**, 2385 (2000).
- ¹⁶M. Copel, E. Cartier, V. Narayanan, M. C. Reuter, S. Guha, and N. Bojarczuk, Appl. Phys. Lett. **81**, 4227 (2002).
- ¹⁷M. Copel, Appl. Phys. Lett. **82**, 1580 (2003).
- ¹⁸S. Stemmer, D. O. Klenov, Z. Chen, D. Niu, W. Ashcraft, and G. N. Parsons, Appl. Phys. Lett. **81**, 712 (2002).
- ¹⁹W. M. Cranton, D. M. Spink, R. Stevens, and C. B. Thomas, Thin Solid Films **226**, 156 (1993).
- ²⁰R. H. Horng, D. S. Wu, J. W. Yu, and C. Y. Kung, Thin Solid Films **289**, 234 (1996).
- ²¹J. J. Araiza, M. A. Aguilar-Frutos, and C. Falcony, J. Vac. Sci. Technol. B **19**, 2206 (2001).
- ²²E. K. Evangelou, C. Wiemer, M. Fanciulli, M. Sethu, and W. Cranton, J. Appl. Phys. **94**, 318 (2003).
- ²³S. C. Choi, M. H. Cho, S. W. Whangbo, C. N. Whang, S. B. Kang, S. I. Lee, and Y. Lee, Appl. Phys. Lett. **71**, 903 (1997).
- ²⁴M.-H. Cho, D.-H. Ko, K. Jeong, S. W. Whangbo, C. N. Whang, S. C. Choi, and S. J. Cho, J. Appl. Phys. **85**, 2909 (1999).
- ²⁵S.-K. Kang, D.-H. Ko, E.-H. Kim, M. H. Cho, and C. N. Whang, Thin Solid Films **353**, 8 (1999).
- ²⁶R. J. Gaboriaud, F. Pailloux, P. Guerin, and F. Paumier, Thin Solid Films **400**, 106 (2001).
- ²⁷F. Paumier and R. J. Gaboriaud, Thin Solid Films **441**, 307 (2003).
- ²⁸M.-H. Cho, D.-H. Ko, Y. G. Choi, K. Jeong, I. W. Lyo, D. Y. Noh, H. J. Kim, and C. N. Whang, J. Vac. Sci. Technol. A **19**, 192 (2001); M.-H. Cho, D.-H. Ko, Y. G. Choi, I. W. Lyo, K. Jeong, C. N. Whang, H. J. Kim, and D. Y. Noh, *ibid.* **19**, 200 (2001).
- ²⁹N. Bassim, V. Cracium, J. Howard, and R. K. Singh, Appl. Surf. Sci. **205**, 267 (2003).
- ³⁰J. Kwo *et al.*, Appl. Phys. Lett. **77**, 130 (2000).
- ³¹J. Kwo *et al.*, J. Appl. Phys. **89**, 3920 (2001).
- ³²T. S. Lay, Y. Y. Liao, W. D. Liu, Y. H. Lai, W. H. Hung, J. Kwo, M. Hong, and J. P. Mannaerts, Solid-State Electron. **47**, 1021 (2003).
- ³³A. C. Rastogi and R. N. Sharma, Appl. Phys. A: Mater. Sci. Process. **77**, 93 (2003).
- ³⁴S. Guha, E. Cartier, M. A. Gribelyuk, N. A. Bojarczuk, and M. C. Copel, Appl. Phys. Lett. **77**, 2710 (2000).
- ³⁵G. Apostolopoulos, G. Vellianitis, A. Dimoulas, M. Alexe, R. Scholz, M. Fanciulli, D. T. Dekadjevi, and C. Wiemer, Appl. Phys. Lett. **81**, 3549 (2002).
- ³⁶Y. Tsuchiya, M. Endoh, M. Kurosawa, R. T. Tung, T. Hattori, and S. Oda, Jpn. J. Appl. Phys., Part 1 **42**, 1957 (2003).
- ³⁷J. P. Sénateur, R. Madar, F. Weiss, O. Thomas, and A. Abrutis, French Patent No. FR 2707671 (1993), European Patent No. EP 730671 (1994), U.S. Patent No. US 945162 (1999).
- ³⁸F. Felten, J. P. Sénateur, F. Weiss, R. Madar, and A. Abrutis, J. Phys. IV **5**, C5-1079 (1995).
- ³⁹C. Dubourdieu, J. P. Sénateur, and F. Weiss, *Crystal Growth in Thin Solid Films: Control of Epitaxy*, edited by M. Guilloix-Viry and A. Perrin (Research Signpost, Kerala, 2002), ISBN 81-7736-095-7, p. 169.
- ⁴⁰K.-J. Choi, W.-C. Shin, and S.-G. Yoon, J. Electrochem. Soc. **149**, F18 (2002).
- ⁴¹K.-J. Choi, J.-B. Park, and S.-G. Yoon, J. Electrochem. Soc. **150**, F75 (2003).
- ⁴²B.-O. Cho, J. Wang, and J. P. Chang, J. Appl. Phys. **92**, 4238 (2002).
- ⁴³D. Niu, R. W. Ashcraft, Z. Chen, S. Stemmer, and G. N. Parsons, J. Electrochem. Soc. **150**, F102 (2003).
- ⁴⁴H. Kato, T. Nango, T. Miyagawa, T. Katagiri, K. S. Seol, and Y. Ohki, J. Appl. Phys. **92**, 1106 (2002).
- ⁴⁵J. Koo, Y. Kim, and H. Jeon, Jpn. J. Appl. Phys., Part 1 **41**, 3043 (2002).
- ⁴⁶Y. Kim, J. Koo, J. Han, S. Choi, H. Jeon, and C.-G. Park, J. Appl. Phys. **92**, 5443 (2002).
- ⁴⁷J. H. Lee, Y. J. Cho, Y. S. Min, D. Kim, and S. W. Rhee, J. Vac. Sci. Technol. A **20**, 1828 (2002).
- ⁴⁸Z. H. Lu, J. P. McCaffrey, B. Brar, G. D. Wilk, R. M. Wallace, L. C. Feldman, and S. P. Tay, Appl. Phys. Lett. **71**, 2764 (1997).
- ⁴⁹*Handbook of x-ray Photoelectron Spectroscopy*, edited by J. Chastain (Perkin-Elmer Corporation, Eden Prairie, MN, 1992).
- ⁵⁰M. D. Ulrich, J. E. Rowe, D. Niu, and G. N. Parsons, J. Vac. Sci. Technol. B **21**, 1792 (2003).
- ⁵¹J. F. Moulder, W. F. Stickle, P. E. Sobol, and K. D. Bomben, *Handbook of x-ray Photoelectron Spectroscopy* (Perkin-Elmer Corporation, Eden Prairie, MN, 1992).
- ⁵²M. L. Green, E. P. Gusev, R. Degraeve, and E. L. Garfunkel, J. Appl. Phys. **90**, 2057 (2001).
- ⁵³O. Renault, L. G. Gosset, D. Rouchon, and A. Ermolieff, J. Vac. Sci. Technol. A **20**, 1867 (2002).
- ⁵⁴C. Durand, C. Vallée, C. Dubourdieu, M. Bonvalot, E. Gautier, and O. Joubert, Mater. Res. Soc. Symp. Proc. **786**, E6.15 (2003).
- ⁵⁵J. McPherson, J. Kim, A. Shanware, H. Mogul, and J. Rodriguez, Tech. Dig. - Int. Electron Devices Meet. **2002**, 26, 633; J. McPherson, J.-Y. Kim, A. Shanware, and H. Mogul, Appl. Phys. Lett. **82**, 2121 (2003).